nature chemical biology

Article

https://doi.org/10.1038/s41589-022-01193-2

A potent and broad neutralization of SARS-CoV-2 variants of concern by DARPins

Received: 19 February 2022

Accepted: 30 September 2022

Published online: 21 November 2022

Check for updates

Vikas Chonira[1], Young D. Kwon[2,10], Jason Gorman[2,10], James Brett Case[3,10], Zhiqiang Ku[4,10], Rudo Simeon[1], Ryan G. Casner[5], Darcy R. Harris[2], Adam S. Olia[2], Tyler Stephens[6], Lawrence Shapiro[5], Michael F. Bender[2], Hannah Boyd[4], I-Ting Teng[2], Yaroslav Tsybovsky[6], Florian Krammer[7,8], Ningyan Zhang[4], Michael S. Diamond[3,9] ✉, Peter D. Kwong[2] ✉, Zhiqiang An[4] ✉ & Zhilei Chen[1] ✉

We report the engineering and selection of two synthetic proteins—FSR16m and FSR22—for the possible treatment of severe acute respiratory syndrome coronavirus 2 (SARS-CoV-2) infection. FSR16m and FSR22 are trimeric proteins composed of DARPin SR16m or SR22 fused with a T4 foldon. Despite selection by a spike protein from a now historical SARS-CoV-2 strain, FSR16m and FSR22 exhibit broad-spectrum neutralization of SARS-CoV-2 strains, inhibiting authentic B.1.351, B.1.617.2 and BA.1.1 viruses, with respective IC_{50} values of 3.4, 2.2 and 7.4 ng ml^{-1} for FSR16m. Cryo-EM structures revealed that these DARPins recognize a region of the receptor-binding domain (residues 456, 475, 486, 487 and 489) overlapping a critical portion of the angiotensin-converting enzyme 2 (ACE2)-binding surface. K18-hACE2 transgenic mice inoculated with B.1.617.2 and receiving intranasally administered FSR16m showed less weight loss and 10–100-fold lower viral burden in upper and lower respiratory tracts. The strong and broad neutralization potency makes FSR16m and FSR22 promising candidates for the prevention and treatment of infection by SARS-CoV-2.

Severe acute respiratory syndrome coronavirus 2 (SARS-CoV-2) has infected over 628 million people worldwide resulting in over 6.6 million deaths as of October 2022 (ref. [1]). Multiple SARS-CoV-2 variants with increased infectivity have emerged, which jeopardize the utility of current vaccines and therapeutic antibodies. Although several monoclonal antibody (mAb) therapeutics have received emergency use authorization and demonstrated efficacy in patients, they are limited by high production cost, global supply issues and inconvenient routes of administration[2]. In addition, many human-derived mAbs have shown reduced efficacy against newly evolved viral variants[3].

In this article, we report the engineering and characterization of two highly potent and broadly neutralizing synthetic proteins,

[1]Department of Microbial Pathogenesis and Immunology, Texas A&M University Health Science Center, Bryan, TX, USA. [2]Vaccine Research Center, National Institute of Allergy and Infectious Diseases, National Institutes of Health, Bethesda, MD, USA. [3]Department of Medicine, Washington University School of Medicine, Saint Louis, MO, USA. [4]Texas Therapeutics Institute, Brown Foundation Institute of Molecular Medicine, The University of Texas Health Science Center at Houston, Houston, TX, USA. [5]Department of Biochemistry and Molecular Biophysics, Columbia University, New York, NY, USA. [6]Vaccine Research Center Electron Microscopy Unit, Cancer Research Technology Program, Leidos Biomedical Research Inc, Frederick National Laboratory for Cancer Research, Frederick, MD, USA. [7]Department of Microbiology, Icahn School of Medicine at Mount Sinai (ISMMS), New York City, NY, USA. [8]Department of Pathology, Molecular and Cell based Medicine, ISMMS, New York City, NY, USA. [9]Department of Pathology and Immunology, Department of Molecular Microbiology, and The Andrew M. and Jane M. Bursky Center for Human Immunology and Immunotherapy Programs, Washington University School of Medicine, Saint Louis, MO, USA. [10]These authors contributed equally: Young D. Kwon, Jason Gorman, James Brett Case, Zhiqiang Ku. ✉e-mail: mdiamond@wustl.edu; pkwong@mail.nih.gov; zhiqiang.an@uth.tmc.edu; zchen4@tamu.edu

https://doi.org/10.1038/s41589-022-01193-2

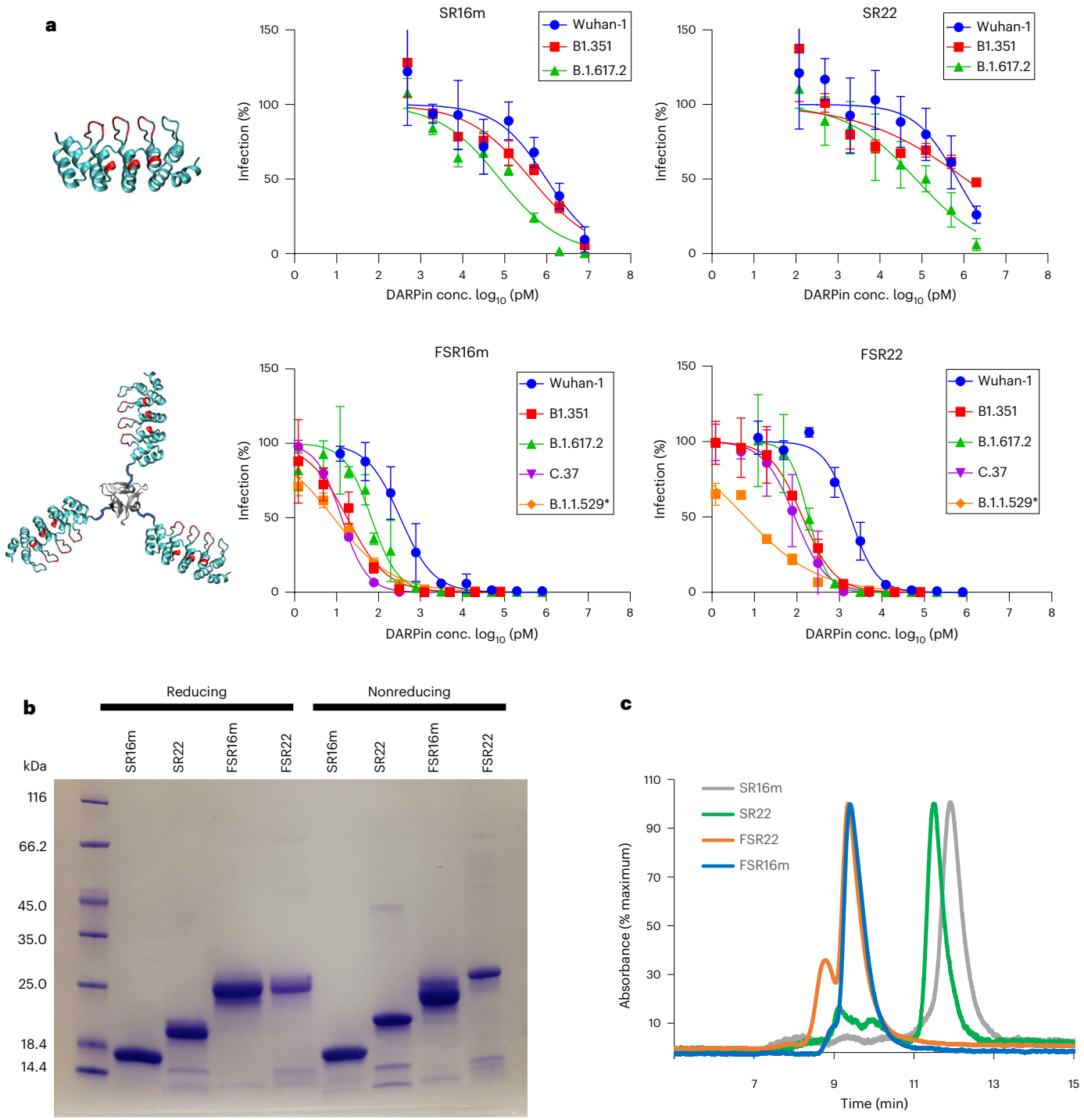

Fig. 1 | Neutralization of spike protein pseudotyped lentiviruses. a, Illustration of the engineered monomeric and trimeric DARPin molecules and their neutralization of pseudotyped lentiviruses. B.1.1.529* harbors a chimeric spike protein in which the RBD region (residue, 338–514) of B.1.351 was replaced with that from B.1.1.529 (BA.1). Residues in red were randomized during DARPin engineering. Data points are shown as mean ± s.d. from at least two independent experiments. **b**, SDS–PAGE gel analysis of the DARPin molecules under nonreducing and reducing conditions. The gel image was representative of three independent experiments. **c**, Size-exclusion chromatography of DARPin molecules under nonreducing conditions. The chromatograph was representative of two experiments.

FSR16m and FSR22, as candidates for preventing and treating coronavirus disease 2019 (COVID-19). The active domains of FSR16m and FSR22 are designed ankyrin repeat proteins (DARPins) engineered to mimic human angiotensin-converting enzyme 2 (hACE2) binding to the receptor-binding domain (RBD) of the spike protein. DARPin is a versatile synthetic binder scaffold that has high thermostability and has been engineered to bind an array of targets with pico- to nanomolar affinities[4,5], including the SARS-CoV-2 spike protein[6]. Trimerization of RBD-binding DARPins SR16m and SR22 with a T4 foldon[7] molecule increased their neutralization potency by >300-fold. Remarkably, and despite using the Wuhan-1 historical isolate spike protein as the target of engineering, both FSR16m and FSR22 exhibit substantially enhanced neutralization potency against a panel of SARS-CoV-2 variants of interest (VOI) and variants of concern (VOC) relative to the ancestral virus

Table 1 | Summary of the neutralization IC_{50} values in Fig. 1a

IC_{50}	WT	B.1.351 (beta)	B.1.617.2 (delta)	C.37 (lambda)	B.1.1.529* (omicron*)
SR16m	1 μM	0.42 μM	77.8 nM	N.D.	N.D.
SR22	0.7 μM	1.1 μM	71.4 nM	N.D.	N.D.
FSR16m	23.7 ng ml^{-1}	1.3 ng ml^{-1}	4.8 ng ml^{-1}	0.9 ng ml^{-1}	0.6 ng ml^{-1}
	331 pM	18 pM	67 pM	13 pM	8.5 pM
FSR22	130 ng ml^{-1}	9.5 ng ml^{-1}	13.3 ng ml^{-1}	6.3 ng ml^{-1}	0.6 ng ml^{-1}
	1834 pM	135 pM	188 pM	89 pM	7.3 pM

in pseudovirus assays. Cryo-electron microscopy (cryo-EM) studies confirmed that both SR16m and SR22 target an essential ACE2-binding epitope on the RBD, providing support for the idea that these DARPins may remain effective against future SARS-CoV-2 variants. Although the improvement in neutralization potency against some newly emerged viral variants was not built into our DARPins design, the broad-spectrum activity is a direct result of our engineering approach that combines protein trimerization to increase avidity with the selection of DARPins that can compete with the viral receptor (that is, hACE2).

Results

Engineering of FSR16m and FSR22

Employing an in-house DARPin library with >10^9 distinct clones displayed on M13 phage particles, we sequentially enriched binders to biotinylated RBD and the full-length spike protein (Wuhan-1 strain) over four rounds of phage panning (Supplementary Fig. 1). The enriched DARPin library pool from the final round was cloned into an expression vector with 6xHis and Myc tags at the N-terminus and transformed into BL21(DE3) *Escherichia coli* cells. Three hundred colonies were picked and grown in 96-well plates, and the cell lysate was subjected to enzyme-linked immunosorbent assay (ELISA)-based screens. Eleven unique clones bound strongly to both the RBD and the full-length spike protein and were purified by nickel-affinity chromatography. A competition ELISA was used to identify DARPin molecules that could inhibit binding between hACE2 and spike proteins and yielded two unique clones: SR16 and SR22. Sodium dodecyl sulfate-polyacrylamide gel electrophoresis (SDS–PAGE) analysis of these proteins revealed a homogenous band for SR22 and an additional band for SR16 (Supplementary Fig. 2). The N-terminal 6xHis tag in SR16 was moved to the C-terminus to give rise to SR16m.

Because the SARS-CoV-2 spike protein adopts a trimeric structure, we trimerized both SR16m and SR22 through fusion to a T4 foldon[7], a small trimeric protein, with a flexible (GGGGSLQ)x2 linker to form FSR16m and FSR22 (Supplementary Fig. 3). These trimeric DARPins should bind the spike protein with much higher avidity. Subsequently, using lentiviruses pseudotyped with the Wuhan-1 spike protein, we determined the neutralization activity of SR16m and SR22. Monomeric SR16m and SR22 showed weak inhibitory activity against the historical Wuhan-1 virus with 50% inhibitory concentration (IC_{50}) values of 1 and 0.7 μM, respectively, which were dramatically enhanced upon trimerization (Fig. 1a and Table 1). Despite the use of the Wuhan-1 spike protein during DARPin engineering, both FSR16m and FSR22 exhibited greater neutralization activity toward viruses pseudotyped with spike proteins from VOCs. As an example, the IC_{50} values of FSR16m and FSR22 against pseudoviruses displaying the RBD from the Omicron variant are 8.5 and 7.3 pM, respectively, which are substantially more potent than toward viruses displaying Wuhan-1 spike protein (331 pM and 1.8 nM, respectively).

All monomeric and trimeric DARPin proteins were efficiently expressed in *E. coli* and easily purified by one-step immobilized metal affinity chromatography. The presence of surface Cys residues (Supplementary Fig. 3) did not impact the tertiary structure of these proteins (Fig. 1b). Monomeric DARPin SR16m migrated slightly faster than SR22 on SDS–PAGE gel and eluted later on size exclusion chromatography, while their respective trimers had nearly identical size (Fig. 1b,c). FSR16m was homogenous in solution, whereas a small percentage of FSR22 appeared to aggregate under nonreducing conditions (Fig. 1c).

FSR16m and FSR22 bind diverse RBD variants with high avidity

FSR16m exhibited superior binding avidity than FSR22 against a panel of spike proteins from VOC and VOI (Fig. 2a and Supplementary Fig. 4) in a biolayer interferometry binding assay. Due to the negligible dissociation rate, the K_{Dapp} values of FSR16m for the RBD of Wuhan-1 and six viral variants were below the detection limit (K_{Dapp} < 1 pM). In the case of Omicron RBD, a faster dissociation rate was observed, resulting in K_{Dapp} of 3.65 nM. This result contrasted with our neutralization assay in which the FSR16m exhibited improved IC_{50} values against lentiviruses displaying RBD from the Omicron variant compared to Wuhan-1 virus. The difference in the apparent binding avidity may be due to differences in the tertiary conformation of the protein in solution and on the virus. The binding study used dimeric Fc-tagged RBD. FSR22 maintained a similar binding avidity toward all tested RBDs with a slight increase in avidity to the RBD of Omicron (K_{Dapp} = 2.63 nM) compared to Wuhan-1 (K_{Dapp} = 12.3 nM). Overall, a faster dissociation rate was observed for FSR22 than FSR16m.

To assess the breadth of FSR16m and FSR22 interaction with other SARS-CoV-2 VOC and VOI, we determined their binding to a panel of 24 RBD mutants by ELISA. Remarkably, FSR16m maintained nanomolar EC_{50} values toward all variants except for the ones with K417E and F486V/F486S substitutions (Fig. 2c). While the K417E variant was predicted to escape antibody neutralization based on the pseudotyped virus studies[8], this amino acid change also resulted in reduced binding affinity of spike for hACE2 (17.8% of Wuhan-1 control)[9] due to the loss of a critical salt bridge interaction between the positively charged K417 in the spike protein and the negatively charged Asp in hACE2. K417N/K417T substitutions are present in B.1.351 (β) and P.1 (γ) variants (Supplementary Table 1). The affinity of FSR16m for the B.1.351 RBD (K417N + E484K + N501Y, EC_{50} 0.43 nM) is similar to Wuhan-1 RBD (EC_{50} of 0.59 nM) but slightly weaker than that for a variant with only E484K + N501Y (EC_{50} of 0.23 nM), indicating that the K417N mutant weakens the interaction slightly between FSR16m and the spike protein. Similarly, the variants F486V and F486S also exhibit decreased hACE2-binding affinity (37% and 57%, respectively, of Wuhan-1 control[9]). Consequently, variants with these mutations (for example, BA.4/.5) may exhibit reduced viral fitness and virulence. Mutations G476S and G446V enable resistance to neutralization by antibodies REGN-10933 and REGN-10987, respectively[10]. Nonetheless, and despite a greater than 10-fold increase in EC_{50} values, FSR16m still maintained nM binding avidity to spike proteins with both of these variants (Fig. 2c). However, no detectable interaction was observed between FSR16m and the RBD proteins of sarbecoviruses of clade 1a (SARS-CoV-1, RaTG13, WIV1), clade 2 (BtkY72) and clade 3 (Rs4081) using the same binding assay (Supplementary Fig. 5), indicating that the epitope of FSR16m is not conserved among other sarbecoviruses.

FSR22 retained high-avidity binding to most of the tested variants with EC_{50} < 10 nM although its binding strength was generally lower than FSR16m. Similar to FSR16m, FSR22 also exhibits lower avidity to RBDs harboring variants K417E, F486V/F486S, G446V or G476S. Beyond these, FSR22 had reduced avidity to RBDs containing a T478K substitution, pointing to its engagement of a slightly different binding interface than FSR16m. The ability of FSR16m and FSR22 to bind diverse RBD variants with high avidity may stem from our engineering approach, which aimed to identify binders that mimic hACE2 engagement, a step that the virus is obligated to maintain as high-affinity binding for efficient infection.

https://doi.org/10.1038/s41589-022-01193-2

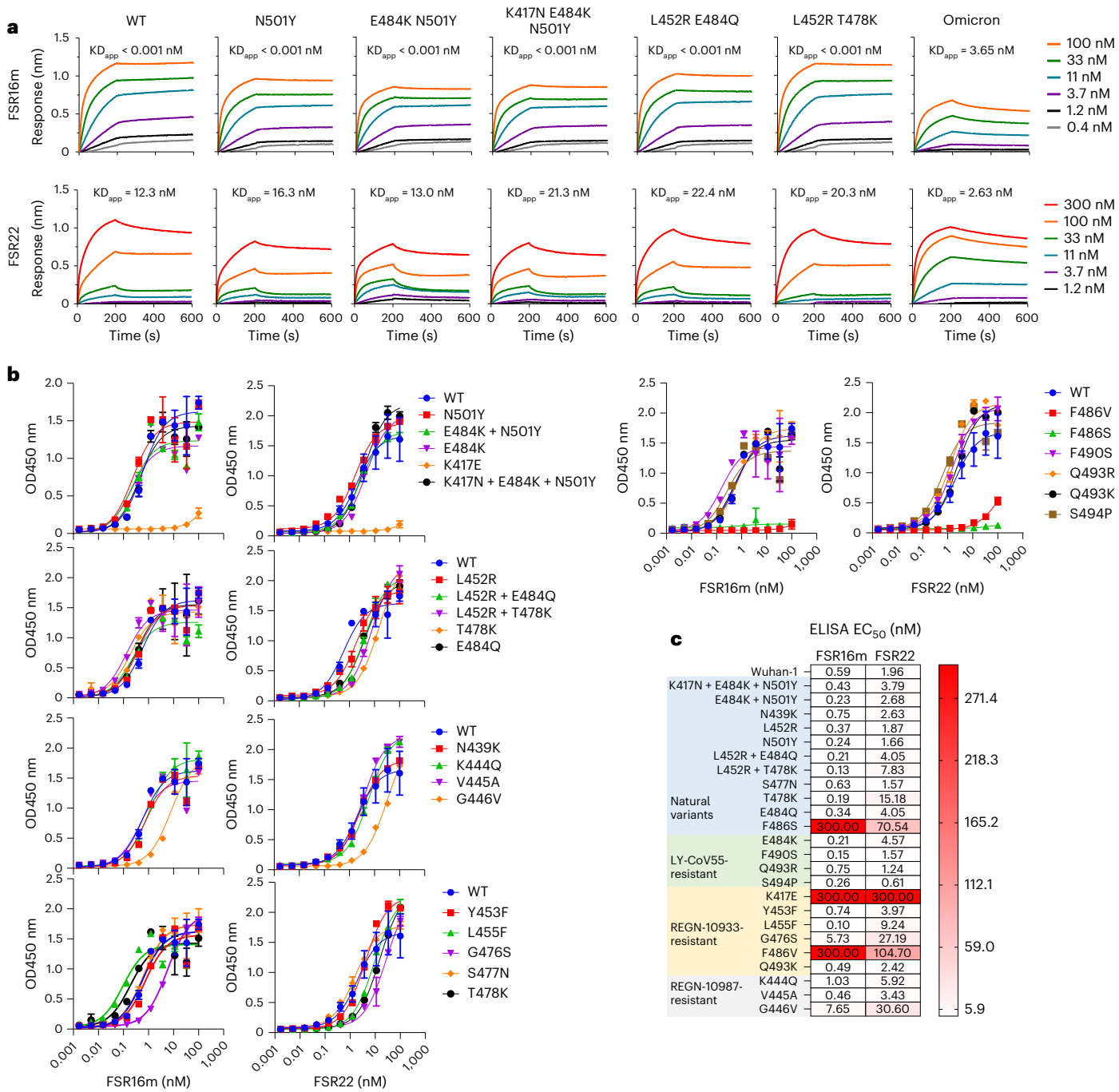

Fig. 2 | FSR16m and FSR22 maintain high avidity toward SARS-CoV-2 variants. **a**, Binding kinetics to selected variant RBD proteins. Each data curve is from one biosensor at indicated time points, and six concentrations were tested in one representative experiment. **b**, ELISA binding titration to a panel of 24 RBD variants. Data points are shown as mean ± s.d. from one representative experiment with two technical replicates. **c**, Summary of the 50% maximum effective binding concentrations (EC_{50}) to RBD proteins with indicated variants. The EC_{50} values are the means of duplicate wells from two independent experiments.

FSR16m and FSR22 neutralize authentic viruses

We next tested the capacity of FSR16m and FSR22 to neutralize authentic SARS-CoV-2 in Vero-hACE2-TMPRSS2 cells[11]. Both FSR16m and FSR22 DARPins efficiently inhibited infection of several authentic SARS-CoV-2 strains (Fig. 3a and Table 2). The IC_{50} values of FSR16m against B.1.351, B.1.617.2 and B.1.617.2.AY1 viruses were 3.4, 2.2 and 3.3 ng ml^{-1}, respectively, values comparable to that of the Regen-COV antibody cocktail[12]. While both DARPins neutralized authentic Omicron strains, FSR16m was more potent. The IC_{50} values of FSR16m and FSR22 against BA.1, BA.1.1 and BA.2 strains were 44.7 and 169.2 ng ml^{-1}, 7.4 and 41.2 ng ml^{-1}, and 33.3 and 216.2 ng ml^{-1}, respectively (Table 2).

Given the potency of FSR16m, we investigated the in vivo efficacy of this DARPin in mice. Eight-week-old female heterozygous K18-hACE2 C57BL/6J[13] mice were administered 10^3 focus-forming units (FFU) of SARS-CoV-2 B.1.617.2 on day 0. This dose of SARS-CoV-2 was determined to cause severe lung infection and inflammation in previous studies[14–16]. On days 1 and 4 post infection, FSR16m (50 µg per mouse in PBS) was administered via an intranasal route. FSR16m-treated mice had less weight loss and 10- to 100-fold lower levels of viral RNA in the lung, heart and nasal wash than mice treated with PBS (Fig. 3b–e). Mice treated with FSR16m also showed lower levels of several proinflammatory cytokines compared to the control-treated, infected mice (Fig. 3f and

https://doi.org/10.1038/s41589-022-01193-2

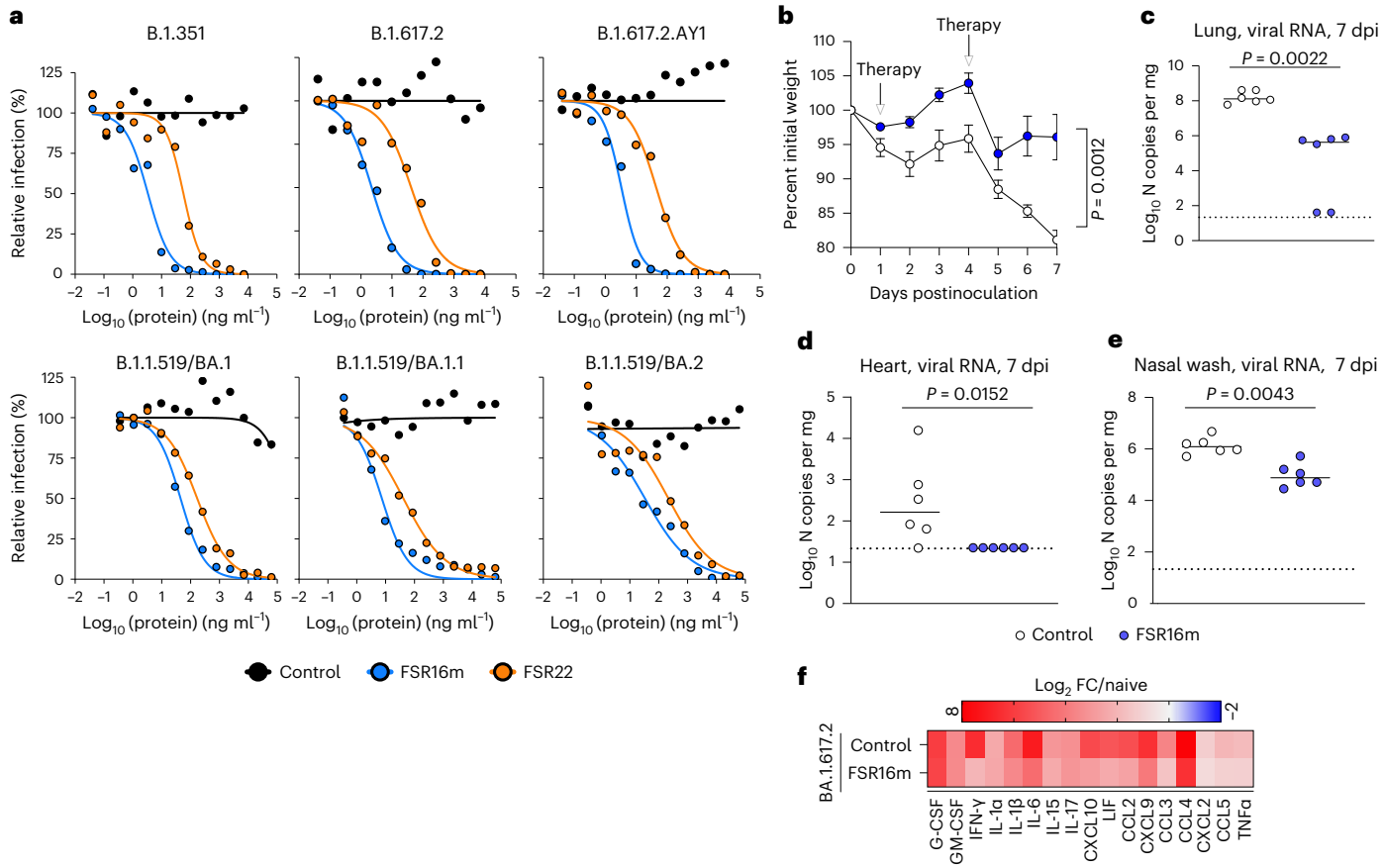

Fig. 3 | Neutralization of authentic SARS-CoV-2 viruses. a, FSR16m and FSR22 potently neutralized authentic SARS-CoV-2 variants. DARPins were incubated with 10^2 FFU of SARS-CoV-2 for 1 h followed by addition to Vero-hACE2-TMPRSS2 cells. One representative experiment with the mean of two technical replicates is shown. **b**–**e**, Intranasally administered FSR16m protected mice against infection by SARS-CoV-2 B.1.617.2. **b**, Weight change following infection with 10^3 FFU of SARS-CoV-2 B.1.617.2 via intranasal administration. Data points are shown as the mean ± s.e.m. from one representative experiment with six technical replicates; Welch's two-tailed *t*-test of the AUC (**c**–**e**) Viral RNA levels at 7 dpi in the lung, heart and nasal wash ($n = 6$, two experiments). Two-tailed Mann–Whitney test, significant *P* values are denoted in the individual panel. **f**, Heat map of cytokine and chemokine protein expression levels in lung homogenates from the indicated groups. Data are presented as $\log_2$-transformed fold-change (FC) over naive mice. Blue, reduction; red, increase. Results are from two experiments.

Supplementary Fig. 6). Thus, FSR16m showed post exposure therapeutic efficacy against SARS-CoV-2 as an intranasally administered protein.

Cryo-EM structures of DARPin in complexes with SARS-CoV-2 spike

To understand the broadly neutralizing activity of FSR22 and FSR16m against SAR-CoV-2 variants, we determined their cryo-EM structures in complex with SARS-CoV-2 S 6P spike proteins[17]. Ab initio reconstructions of cryo-EM images of the complexes followed by heterogeneous refinements revealed trimeric SARS-CoV-2 spikes with a variety of RBD conformations, ranging from all RBD-down to one, two or three RBD-up conformations—with SR22 or SR16m binding to the RBD-up forms in all cases (Supplementary Fig. 7). As FSR22 and FSR16m, the trimeric forms of three SR22 or SR16m linked by a foldon were the most inhibitory, we focused on refining the three RBD-up conformations of SARS-CoV-2 spikes with the FSR22 (or FSR16m) bound to the tip of the RBD in its open conformation (Fig. 4a,b, Supplementary Figs. 8, 9 and Supplementary Table 2). While the trimeric spike complexes were generally well-defined, the tip of the RBD along with FSR22 (or FSR16m) showed substantial conformational heterogeneity. As a result, we could not delineate the FSR22 (or FSR16m)-RBD interface in atomic detail, even after extensive heterogeneous refinement followed by local refinement (Supplementary Figs. 8 and 9). The overall fold of the DARPins and the tip of the RBDs did, however, fit well, and these revealed both FSR22 and FSR16m to bind at the 'tip' of the RBD in their 'RBD-up' conformation (Fig. 4a–d).

Table 2 | Summary of neutralization IC_{50} values against authentic SARS-CoV-2 viruses in Fig. 3a

IC_{50} (ng ml^{-1})	B.1.351	B.1.617.2	B.1.617.2/AY1	B.1.1.519/BA.1	B.1.1.519/BA.1.1	B.1.1.519/BA.2
FSR16m	3.4	2.2	3.3	44.7	7.4	33.3
FSR22	57.2	41.7	44.2	169.2	41.2	216.2

Although the FSR22 structure in complex with SARS-CoV-2 spike was determined at slightly higher resolution than the FSR16m structure (Supplementary Figs. 8 and 9), the conformational mobility of these structures reduced their resolution. To corroborate our findings, we determined structures of these DARPin molecules in complex with RBD by itself. To provide sufficient mass for cryo-EM structure determination, we added the antigen-binding fragments (Fabs) from two antibodies (S309 and CR3022) that neither compete with each other nor with either DARPin molecule (Supplementary Figs. 10–12 and Supplementary Table 2). We obtained a structure of the quaternary complex with SR22 at 4.11 Å resolution, with density for the DARPin of similar quality as RBD and Fab variable domains (Supplementary Fig. 11); we also obtained a structure of the quaternary complex with SR16m at 4.26 Å resolution, where the slightly reduced resolution related to the propensity of SR16m to self-aggregate (Supplementary Fig. 12). Despite differences in trimerization (with

https://doi.org/10.1038/s41589-022-01193-2

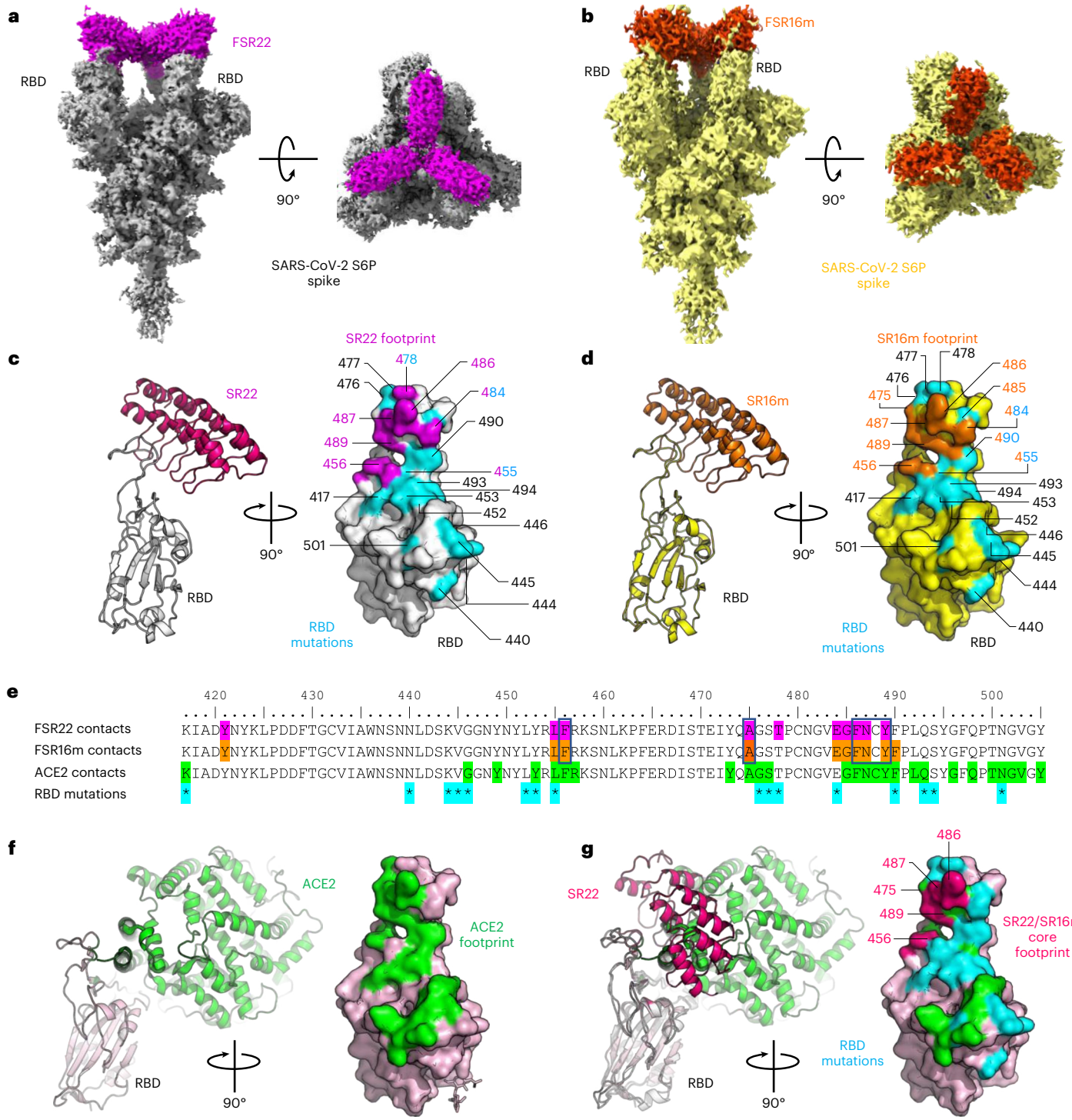

Fig. 4 | Cryo-EM structures of DARPins in complexes with SARS-CoV-2 spike. a, Cryo-EM map of FSR22 (magenta)-bound SARS-CoV-2 S 6P spike in its RBD-open conformation. **b**, cryo-EM map of FSR16m (orange)-bound SARS-CoV-2 S 6P spike. **c**, SR22-bound RBD in cartoon representation (left). The footprint of SR22 on the surface of RBD (gray) was shown in magenta (right). RBD residues that underwent mutations in VOCs were highlighted in cyan (right). **d**, SR16m-bound RBD in cartoon representation (left). The footprint of SR16m on the surface of RBD (yellow) was shown in orange (right). **e**, Amino acid residues of RBD contacting FSR22, FSR16m and ACE2 were highlighted in magenta, orange and green, respectively. Amino acid residues of RBD that underwent mutations in VOCs were denoted with an asterisk (*). '**' and '***' are multiples of '*'. Amino acid residues of RBD that form a core footprint of monomeric and trimeric DARPins were highlighted with rectangular boxes. **f**, ACE2-bound RBD was in cartoon representation (PDB: 7C8D) (left panel). The ACE2 footprint on RBD was highlighted in green (right). **g**, Overlay of SR22-bound RBD and ACE2-bound RBD structure (left). Overlay of footprints of ACE2, SR22 and SR16m core and RBD residues underwent mutations in the VOCs (right).

either spike/RBD or trimeric/monomeric DARPin), the overall fold of the two DARPins and their binding mode to SARS-CoV-2 were nearly identical.

The four structures suggested that the DARPins recognize a subset of RBD surface composed of residues F456, A475, F486, N487 and Y489, which overlap closely with the hACE2-binding surface[18,19]

(Fig. 4e). Notably, most of these residues did not overlap with residues that changed in VOC, including N501Y in B.1.1.7 (Alpha), K417N, E484K and N501Y in B.1.351 (Beta), L452R and E484Q in B.1.617.2 (Gamma), and K417N, S477N, Q498R and N501Y in B.1.1.529 (Omicron) (Fig. 4e–g), suggesting that the surface recognized by FSR22 (or FSR16m) is important for ACE2 binding, and changes in these residues may compromise viral infectivity and fitness[19]. Comparison of the two DARPin-RBD complexes and the ACE2-RBD structure revealed a steric clash between a monomer of SR22 (or SR16m) and ACE2 bound to RBD, as the DARPins and ACE2 recognize overlapping binding surfaces (Fig. 4f,g). However, SR22 and SR16m only buried approximately 500 Å^2 of surface area on RBD, whereas ACE2 binding buried approximately 970 Å^2 of the surface on RBD, explaining the structural basis for the relatively poor neutralizing ability of SR22 and SR16m (monomers) as they could be outcompeted by ACE2 for RBD binding (Fig. 4f,g). Conversely, FSR22 and FSR16m, composed of three SR22 and SR16m, respectively, can overcome the lower affinity of monomeric DARPins to RBD by binding three RBDs in their open conformation (Fig. 4a,b). Collectively, the cryo-EM structures of FSR22 and FSR16m-bound SARS-CoV-2 spike revealed that FSR22 and FSR16m potently neutralize SARS-CoV-2 including VOCs by targeting a minimal but essential subset of ACE2-binding residues and taking advantage of avidity gained by trimerization.

Discussion

By using phage panning coupled with functional screening, we report the engineering of DARPins with potent and broad neutralization activity against SARS-CoV-2. Monomeric DARPin SR16m and SR22 exhibited weak viral neutralization potency, but this was dramatically enhanced upon trimerization by fusion with a T4 foldon. Although the Wuhan-1 spike protein was used for engineering, FSR22 and FSR16m exhibited substantially increased neutralization potency against newer viral variants.

Our cryo-EM structural analysis revealed that both FSR22 and FSR16m recognize a distinct region of the ACE2-binding surface on RBD, particularly residues 421, 456 and 485–489. Shang et al. demonstrated that mutation of residues 481–489 reduced ACE2 binding substantially[19], and Starr et al. reported that muations in residues 421, 475 and 487 reduced RBD expression and possibly viral fitness, whereas mutations in residues 421, 456, 475, 486, 487 and 489 reduced ACE2-binding affinity[9]. The precise targeting of essential ACE2 interacting residues on RBD by FSR22 and FSR16m may explain their pan-neutralization of naturally derived SARS-CoV-2 variants, and our two DARPins may effectively prevent infection of variants that require hACE2 for entry.

The ability of these DARPins to exhibit increased neutralization potency toward SARS-CoV-2 variants contrasts with many human-derived anti-SARS-CoV-2 mAbs, which lose neutralization potency[3]. The following reasons may account for this phenomenon: (a) naturally derived viral variants are selected in part by their ability to evade population immunity (either through vaccination or natural infection)[3]. This contrasts with in vitro engineered DARPins whose potency appears to be less affected by the virus evolution history. (b) The dimeric structure of an antibody limits a maximum of two spike proteins within a spike trimer to be simultaneously engaged by a single antibody, necessitating a high affinity between the antibody and the spike protein and a close match of the binding interface. Even small changes at or near the binding interface could disrupt antibody-spike protein interactions and reduce the antibody binding and neutralization potency. In contrast, due to its much smaller size, a trimer DARPin can easily engage all three monomers in a spike trimer concurrently. The strong avidity effect from the trimer interaction can compensate for the weak binding affinity of the monomer and enable the trimers to tolerate variants at or near the binding interface without compromising potency. (c) DARPins SR16 and SR22 were selected based on their ability to compete with hACE2 for binding to the spike protein rather than their ability to inhibit viral infection. An effective way to inhibit ACE2 binding to spike is to occupy the interface for hACE2 binding, and indeed both DARPins engage key residues within the hACE2-binding interface. As emerging natural VOCs tend to exhibit higher infectivity and ACE2 binding affinity[20–22], these variants may become more susceptible to binding and neutralization by our DARPin molecules.

The upper airway epithelium is the first site of infection by SARS-CoV-2 due in part to its robust expression of hACE2 (ref. [23]). Infected upper airway epithelium cells release progeny viruses, which lead to infection of other organs including the lung. Antibody therapeutics have been an effective weapon for treating COVID-19, with several virus-neutralizing IgG antibodies approved for emergency use by the Food and Drug Administration[24–26]. However, antibodies have several limitations as therapeutics for treating SARS-CoV-2: (a) antibody production requires sophisticated mammalian cell culture and is expensive and suffers from limited global manufacturing capacity; (b) IgG antibody requires subcutaneous or intravenous routes of administration that may be inconvenient or impractical for some patients and care providers; (c) intravenously and subcutaneously administered antibodies have poor access to mucosal compartments with an estimated 50- to 100-fold lower antibody levels than in blood[27–29], necessitating a high therapeutic dose and (d) many current COVID-19 antibody therapeutics have a narrow neutralization spectrum and require cocktails to maintain efficacy toward newly emerged SARS-CoV-2 variants.

Through the use of the stringent K18-hACE2 mouse model of SARS-CoV-2 pathogenesis, we showed that intranasal administration of FSR16m on days 1 and 4 post infection reduced viral burden and weight loss. As several other studies have demonstrated[14,30–32], overexpression of hACE2 in these mice results in severe lung inflammation and disease upon infection with SARS-CoV-2. Therefore, the level of protection we observed by intranasal administration of FSR16m is significant. However, the current format of intranasal delivery likely is not directly translatable to humans due to limited lung exposure. Several protein-based antivirals are currently under development against COVID-19 (refs. [29,33–35]). However, unlike FSR16m, which potently neutralized all tested VOCs, many of these have narrower spectrum of neutralization. FSR16m is efficiently expressed in *E. coli* (>200 mg per liter of shaker flask culture, on par with that reported previously[36]), enabling its cost-effective production on a large scale. In addition, FSR16m exhibits remarkable stability with <10-fold loss in activity after storage at room temperature for 6 weeks (Supplementary Fig. 13), consistent with the previously reported DARPin storage stability[37] and making the molecule a promising therapeutic candidate.

Previously, two highly potent anti-SARS-CoV-2 hetero-trimeric DARPin molecules, MM-DC (MP0420, ensovibep) and MR-DC (MP0423), were reported[6]. Both DARPins exhibited picomolar IC_{50} values against spike protein pseudotyped vesicular stomatitis virus particles and were 10–50-fold more potent than their constituent monomer DARPins. This level of potency enhancement contrasts with both FSR16m and FSR22, whose IC_{50} values improved >300-fold upon homo-trimerization. When administered via intraperitoneal route at 10 mg kg^{-1}, MR-DC reduced the viral load in nasal turbinates and lung by ~10 and ~100-fold, respectively[38]. A similar level of viral load reduction in these tissues was achieved by intranasally administered FSR16m at 2.5 mg kg^{-1} per animal. Both MM-DC and MR-DC are pentameric molecules composed of two albumin-binding DARPins and three spike-binding DARPins and have a half-life of 4–6 days in hamsters. Intravenously administered MM-DC reduced the risk of hospitalization by 78% in phase 2 clinical trial[39]. Although FSR16m and FSR22 in their current form are expected to have a short half-life in vivo and are not suitable for systematic application, the same albumin binding DARPin molecules can be fused to FSR16m to extend its in vivo half-life and make it suitable for intravenous application.

In summary, we report the engineering of two homotrimeric DARPin molecules, FSR16m and FSR22, with potent and broad SARS-CoV-2 neutralization activity. Both proteins are amenable to rapid

and cost-effective production in *E. coli*, and intranasally administered FSR16m protected mice previously infected with SARS-CoV-2, suggesting that these proteins might be effective countermeasure candidates for COVID-19. Finally, our work suggests that homo-multimerization of monomeric proteins with moderate antiviral activity may represent an effective strategy for generating broadly neutralizing antiviral agents.

Online content

Any methods, additional references, Nature Research reporting summaries, source data, extended data, supplementary information, acknowledgements, peer review information; details of author contributions and competing interests; and statements of data and code availability are available at https://doi.org/10.1038/s41589-022-01193-2.

References

1. Our World in Data. Coronavirus data explorer: https://ourworldindata.org/explorers/coronavirus-data-explorer
2. Ledford, H. Antibody therapies could be a bridge to a coronavirus vaccine—but will the world benefit? *Nature* **584**, 333–334 (2020).
3. Cao, Y. et al. Omicron escapes the majority of existing SARS-CoV-2 neutralizing antibodies. *Nature* **602**, 657–663 (2022).
4. Stumpp, M. T., Dawson, K. M. & Binz, H. K. Beyond antibodies: the DARPin drug platform. *BioDrugs* **34**, 423–433 (2020).
5. Pluckthun, A. Designed ankyrin repeat proteins (DARPins): binding proteins for research, diagnostics, and therapy. *Annu. Rev. Pharm. Toxicol.* **55**, 489–511 (2015).
6. Rothenberger, S. et al. The trispecific DARPin ensovibep inhibits diverse SARS-CoV-2 variants. *Nat. Biotechnol*. https://doi.org/10.1038/s41587-022-01382-3 (2022).
7. Guthe, S. et al. Very fast folding and association of a trimerization domain from bacteriophage T4 fibritin. *J. Mol. Biol.* **337**, 905–915 (2004).
8. Starr, T. N. et al. Prospective mapping of viral mutations that escape antibodies used to treat COVID-19. *Science* **371**, 850 (2021).
9. Starr, T. N. et al. Deep mutational scanning of SARS-CoV-2 receptor binding domain reveals constraints on folding and ACE2 Binding. *Cell* **182**, 1295–1310 (2020).
10. Plante, J. A. et al. Spike mutation D614G alters SARS-CoV-2 fitness. *Nature* **592**, 116–121 (2021).
11. Case, J. B., Bailey, A. L., Kim, A. S., Chen, R. E. & Diamond, M. S. Growth, detection, quantification, and inactivation of SARS-CoV-2. *Virology* **548**, 39–48 (2020).
12. Chen, R. E. et al. Resistance of SARS-CoV-2 variants to neutralization by monoclonal and serum-derived polyclonal antibodies. *Nat. Med.* **27**, 717–726 (2021).
13. Moreau, G. B. et al. Evaluation of K18-hACE2 mice as a model of SARS-CoV-2 infection. *Am. J. Trop. Med. Hyg.* **103**, 1215–1219 (2020).
14. Winkler, E. S. et al. SARS-CoV-2 infection of human ACE2-transgenic mice causes severe lung inflammation and impaired function. *Nat. Immunol.* **21**, 1327–1335 (2020).
15. Ying, B. et al. Protective activity of mRNA vaccines against ancestral and variant SARS-CoV-2 strains. *Sci. Transl. Med.* **14**, eabm3302 (2022).
16. Hunt, A. C. et al. Multivalent designed proteins neutralize SARS-CoV-2 variants of concern and confer protection against infection in mice. *Sci. Transl. Med.* **14**, eabn1252 (2022).
17. Hsieh, C. L. et al. Structure-based design of prefusion-stabilized SARS-CoV-2 spikes. *Science* **369**, 1501–1505 (2020).
18. Lan, J. et al. Structure of the SARS-CoV-2 spike receptor-binding domain bound to the ACE2 receptor. *Nature* **581**, 215–220 (2020).
19. Shang, J. et al. Structural basis of receptor recognition by SARS-CoV-2. *Nature* **581**, 221–224 (2020).
20. Barton, M.I. et al. Effects of common mutations in the SARS-CoV-2 spike RBD and its ligand, the human ACE2 receptor on binding affinity and kinetics. *ELife* **10**, e70658 (2021).
21. Kuzmina, A. et al. SARS CoV-2 delta variant exhibits enhanced infectivity and a minor decrease in neutralization sensitivity to convalescent or post-vaccination sera. *iScience* **24**, 103467 (2021).
22. Yin, W. et al. Structures of the Omicron spike trimer with ACE2 and an anti-Omicron antibody. *Science* **375**, 1048–1053 (2022).
23. Lee, I. T. et al. ACE2 localizes to the respiratory cilia and is not increased by ACE inhibitors or ARBs. *Nat. Commun.* **11**, 5453 (2020).
24. Hansen, J. et al. Studies in humanized mice and convalescent humans yield a SARS-CoV-2 antibody cocktail. *Science* **369**, 1010–1014 (2020).
25. Chen, P. et al. SARS-CoV-2 neutralizing antibody LY-CoV555 in outpatients with COVID-19. *N. Engl. J. Med.* **384**, 229–237 (2021).
26. Gottlieb, R. L. et al. Effect of bamlanivimab as monotherapy or in combination with etesevimab on viral load in patients with mild to moderate COVID-19: a randomized clinical trial. *JAMA* **325**, 632–644 (2021).
27. Iwasaki, A. Exploiting mucosal immunity for antiviral vaccines. *Annu Rev. Immunol.* **34**, 575–608 (2016).
28. DeFrancesco, L. COVID-19 antibodies on trial. *Nat. Technol.* **38**, 1242–1252 (2020).
29. Loo, Y.M. et al. The SARS-CoV-2 monoclonal antibody combination, AZD7442, is protective in nonhuman primates and has an extended half-life in humans. *Sci. Transl. Med.* **14**, eabl8124 (2022).
30. Oladunni, F. S. et al. Lethality of SARS-CoV-2 infection in K18 human angiotensin-converting enzyme 2 transgenic mice. *Nat. Commun.* **11**, 6122 (2020).
31. Case, J. B. et al. Ultrapotent miniproteins targeting the SARS-CoV-2 receptor-binding domain protect against infection and disease. *Cell Host Microbe* **29**, 1151–1161 (2021).
32. Pinto, D. et al. Cross-neutralization of SARS-CoV-2 by a human monoclonal SARS-CoV antibody. *Nature* **583**, 290–295 (2020).
33. Ku, Z. et al. Nasal delivery of an IgM offers broad protection from SARS-CoV-2 variants. *Nature* **595**, 718–723 (2021).
34. Nambulli, S. et al. Inhalable nanobody (PiN-21) prevents and treats SARS-CoV-2 infections in Syrian hamsters at ultra-low doses. *Sci. Adv.* **7**, eabh0319 (2021).
35. Hoagland, D. A. et al. Leveraging the antiviral type I interferon system as a first line of defense against SARS-CoV-2 pathogenicity. *Immunity* **54**, 557–570 (2021).
36. Binz, H. K. et al. Design and characterization of MP0250, a tri-specific anti-HGF/anti-VEGF DARPin drug candidate. *MAbs* **9**, 1262–1269 (2017).
37. Wang, W. et al. Detection of SARS-CoV-2 in different types of clinical specimens. *JAMA* **323**, 1843–1844 (2020).
38. Walser, M. et al. Highly potent anti-SARS-CoV-2 multi-DARPin therapeutic candidates. bioRxiv, 2020.2008.2025.256339 (2020). https://doi.org/10.1101/2020.08.25.256339
39. DARPins score against COVID-19. *Nat. Biotechnol.* **40**, 285–285 (2022). https://doi.org/10.1038/s41587-022-01266-6

Methods

Selection and screening of spike protein-binding DARPin molecules

An in-house N3C DARPin library with >10^9 diversity was used in the phage panning essentially as described previously[40]. Purified full-length spike protein (BEI NR-52724) and RBD (BEI NR-52306) were biotinylated via EZ-link-sulfo-NHS-LC-biotin (Thermo Fisher Scientific, 21335) and used as target proteins. RBD was used as the target protein in Rounds 1, 2 and 4, while the full-length spike protein was used as the target in Round 3 to ensure the enrichment of DARPins that recognize RBD present on the full-length spike protein. Round 1 used the target protein (100 nM) in solution, whereas Rounds 2–4 employed decreasing concentrations of the target protein immobilized on streptavidin or neutravidin-coated ELISA plates (100, 50 and 20 nM). The enrichment of RBD binding DARPins was confirmed by phage ELISA against both RBD and full-length spike protein following a published protocol[40] (Supplementary Fig. 1).

The enriched DARPin pool from the fourth round was cloned into the pET28a vector for high-level DARPin expression as described previously[41]. The resulting DARPin contains a Myc tag and a 6xHis tag at the N-terminus. After transformation, a total of 300 individual *E. coli* BL21 (DE3) clones were picked and grown in deep 96-well plates (1 ml per well) at 37 °C in Lysogeny broth (LB) and induced with isopropyl-β-D-thiogalactopyranoside (IPTG; 0.5 mM). The next day cell pellets were collected, resuspended in 200 µl of PBS (1.8 mM KH_2PO_4, 10 mM Na_2HPO_4, 137 mM NaCl, 2.7 mM KCl, pH 7.4) and supplemented with lysozyme (200 µg ml^{-1}; Amresco 0663-5G)[41]. An ELISA was used to identify the target binding DARPins. Briefly, Nunc MaxiSorp plates (Thermo Fisher Scientific, 50-712-278) were coated with 4 µg ml^{-1} neutravidin (Thermo Fisher Scientific, 31000) in PBS at room temperature for 2 h. The wells were washed with PBS and then blocked with PBS supplemented with 0.5% BSA (Thermo Fisher Scientific, BP9706100; PBS-B) at 4 °C overnight. The next day, after washing with PBS-T (PBS with 0.1% Tween 20), the wells were incubated with biotinylated RBD or full-length spike protein (20 nM in PBS) at room temperature for 1 h. The wells were washed again with PBS-T before the addition of 100 µl of cell lysate (fivefold diluted in PBS) and incubated at room temperature for 2 h. The amount of plate-bound DARPin in each well was quantified using mouse anti-myc antibody (Invitrogen, 13-2500, 1:2500 diluted in PBS-B) and HRP-conjugated goat antimouse antibody (Jackson ImmunoResearch, 115-035-146; 1:1000 diluted in PBS-B) as the primary and secondary antibodies, respectively, and BioFx TMB (VWR, 100359-154) for color development. In total, 20 and 23 clones showed significant ability to bind to RBD and full-length spike protein, respectively. Sequencing revealed 11 unique clones with significant ability to bind both RBD and full-length spike protein.

To identify DARPin clones able to block spike protein and hACE2 interaction, a competitive ELISA was used[42]. Briefly, the Maxisorp plates were first coated with full-length spike protein (BEI 52308, 2 nM in PBS) at room temperature for 2 h. The wells were blocked with PBS-B at 4 °C overnight, washed with PBS-T, and then incubated with mixtures of hACE2-HRP (prepared in-house, 0.5 nM) and different IMAC-purified DARPins (50 mM)[41,43] at room temperature for 1 h. The amount of hACE2-HRP in each well was quantified using BioFx TMB.

For preparation of hACE2-HRP, hACE2 (Raybiotech, 230-30165; 1.76 mg ml^{-1}) was first biotinylated as described above and then incubated with an equal molar amount of streptavidin-HRP (JIR, 016-030-084) in PBS at room temperature for 20 min and stored at −20 °C in 50% glycerol until use.

Plasmids

Plasmids encoding the wild type Δ19 spike protein were obtained from Addgene (145780). The plasmids for the Δ19 spike protein of B.1.617.2 and C.37 were generously provided by Nathaniel Landau (New York University)[44]. DNA fragment encoding the Δ19 spike protein of strain B. 1.351 and the RBD (residues 339-501) of B.1.1.529 was synthesized by Gene Universal and inserted into the pCG1 plasmid[45]. Paul Bieniasz (The Rockefeller University) provided the 293T cell clone 22 (293T.c22) with high expression efficiency of human ACE2 and the lentiviral reporter plasmid pHIV-1NL4-3-ΔEnv-NanoLuc[46]. The plasmid encoding the chimeric B.1.1.529 spike protein (B.1.1.529*) was constructed by replacing the RBD region (residues 338–514) in B.1.351 with that from B.1.1.529. Briefly, the gBlock fragment of B.1.1.529 RBD was digested with BsaI and BlpI, and ligated to (1) pCG1-B.1.351 backbone digested with BamHI and BlpI and (2) PCR product amplified from the same backbone with primers Spike_F and Spike_R and digested with BamHI and BsaI in a three-fragment-ligation reaction.

gBlock of B.1.1.529 RBD:

Aaaaaaggtctcacttcgatgaggtgttcaatgccaccagattcgcctctgt gtacgcctggaaccggaagcggatcagcaattgcgtggccgactactccgtgctgtacaa cctggccccttttcttcaccttcaagtgctacggcgtgtcccctaccaagctgaacgacctg tgcttcacaaacgtgtacgccgacagcttcgtgatccggggagatgaagtgcggcagat tgcccctggacagacaggcaacatcgccgactacaactacaagctgcccgacgacttca ccggctgtgtgattgcctggaacagcaacaagctggactccaaagtctctggcaactacaa ttacctgtaccggctgttccggaagtccaatctgaagcccttcgagcgggacatctcca ccgagatctatcaggccggcaataagccttgtaacggcgtggccggcttcaactgctactt cccactgagatcctactcctttagacccacatatggcgtgggccaccagccctacagagt ggtggtgctgagcttcgaa

Spike_F: cgaattc*ggatcc*gccacca (Italic letters denote BamHI recognition sequence)

Spike_R: ttttt*ggtctc*tgaaggggcacagattggtga (Italic letters denote BsaI recognition sequence)

To construct trimeric DARPin molecules, the DNA fragment encoding a codon-optimized T4 foldon (Protein Data Bank (PDB): 1RFO) was synthesized by Gene Universal (Newark, DE). T4 foldon was fused to the N-terminus of a DARPin molecule via a flexible (GGGGSLQ)x2 linker and cloned into the pET28a expression vector. DARPin SR16, SR22, FSR16 and FSR22 contain a 6xHis tag and a Myc tag at the N terminus, while SR16m and FSR16m contains only a 6xHis tag at the C terminus (Supplementary Fig. 3).

SARS-CoV-2 spike lentiviral pseudoviruses

Lentiviral pseudoviruses with different SARS-CoV-2 spike proteins ($CoV2_{pp}$) were produced as previously reported[46]. Briefly, plasmids encoding the Δ19 spike protein and reporter pHIV-1NL4-3-ΔEnv-NanoLuc[46] (1:3 molar ratio, 10 µg total) were mixed with 500 µl of serum-free DMEM medium and 44 µl of PEI (1 mg ml^{-1}; Polysciences transporter 5, 26008-5) and used to transfect 5 × 10^6 293T cells seeded the night before. Twenty-four-hour post-transfection, the medium was replaced with fresh DMEM supplemented with 10% FBS and 48-h post-transfection the viral supernatant was collected, aliquoted and stored at −80 °C until use.

To determine the neutralization efficiency, serially diluted DARPin molecules were incubated with $CoV2_{pp}$ (final 500-fold diluted) at 37 °C for 30 min before being added to 293T.c22 cells seeded the night before at 10^4 cells per well in 96-well plates. The plates were incubated at 37 °C/5% CO_2 for 48 h, and the NanoLuc signal from each well was quantified using the Nano-Glo Luciferase Assay kit (Promega, N1120) and a Cytation 5 plate reader equipped with Gen5 3.05 software.

DARPin protein production and characterization

All DARPin molecules were expressed in *E. coli* Bl21 (DE3) cells in LB medium supplemented with 50 µg ml^{-1} of kanamycin. Protein expression was induced with IPTG (0.5 mM) when the culture reached OD600 = 0.5. The protein expression was continued at 37 °C for 5 h, and the cells were collected by centrifugation. The proteins were purified via immobilized metal affinity chromatography (IMAC) using gravity Ni-NTA agarose columns. Protein purity was determined using 12% SDS–PAGE gels.

For in vivo studies, the IMAC-purified FSR16m was sterilized by filtration through a 0.22 µm filter, concentrated and buffer exchanged

into PBS via ultrafiltration (Amicon column MWCO 10 KDa, UFC801024) before endotoxin removal using High-Capacity Endotoxin Removal Spin Columns (Pierce, 88274). The endotoxin level in the protein sample (1.5 mg ml^{-1}) was quantified to be <30 U ml^{-1} using the Pierce Chromogenic Endotoxin Quant Kit (Thermo Fisher Scientific, A39552).

For size exclusion chromatography studies, DARPin samples (0.9 mg ml^{-1} × 0.25 ml) were loaded onto an Enrich SEC 70 × 300 Column equilibrated with PBS (GE AKTApure, with Unicorn 6.3 software). Vitamin B12 (Sigma, V2876-100MG) was used at a final concentration of 1 mg ml^{-1} as an internal control.

Spike RBD and DARPin avidity measurement

The human IgG1 Fc-tagged RBD proteins were made in-house as previously described[33,47]. The avidity measurement was performed on the ForteBio Octet RED 96 system (Sartorius). Briefly, the RBD proteins (20 µg ml^{-1}) were captured onto protein A biosensors for 300 s. The loaded biosensors were then dipped into the kinetics buffer for 10 s for adjustment of baselines. Subsequently, the biosensors were dipped into serially diluted (from 0.13 to 300 nM) DARPin proteins for 200 s to record association kinetics and then dipped into kinetics buffer for 400 s to record dissociation kinetics. Kinetic buffer without DARPin was used to correct the background. Octet Data Acquisition 9.0 software was used to collect affinity data. For fitting of K_D values, Octet Data Analysis software v11.1 was used to fit the curve by a 1:1 binding model using the global fitting method.

ELISA binding assay

ELISA plates were coated with recombinant DARPin protein (2 µg ml^{-1}) at 4 °C overnight and blocked with 5% skim milk at 37 °C for 2 h. One hundred microliters of serially diluted human IgG1 Fc-tagged RBD proteins in 1% skim milk was added to each well, and the plates were incubated at room temperature for 3 h before the addition of 100 µl per well of HRP-conjugated goat anti-human IgG antibody (Jackson ImmunoResearch, 109-035-088; diluted 1:5,000), and the plates were incubated at room temperature for another hour. The plates were washed three to five times with PBS-T (0.05%, Tween 20) between incubation steps. TMB (3,3′,5,5′-tetramethylbenzidine) substrate was added at 100 µl per well for color development. The reaction was stopped by adding 50 µl per well 2 M H_2SO_4. The OD450 nm was read by a SpectraMax microplate reader using Softmax Pro 6.5.1 and analyzed with GraphPad Prism 8.

Cells and authentic viruses

Vero-TMPRSS2 (ref. [48]) and Vero-hACE2-TMPRSS2 (ref. [49]) (a gift of A. Creanga and B. Graham, NIH) were cultured at 37 °C in Dulbecco's Modified Eagle medium (DMEM) supplemented with 10% FBS, 10 mM HEPES pH 7.3, 1 mM sodium pyruvate, 1× nonessential amino acids, 100 U ml^{-1} of penicillin–streptomycin and 5 µg ml^{-1} of puromycin. The B.1.617.2, B.1.617.2.AY1, B.1.351, BA.1, BA.1.1 and BA.2 SARS-CoV-2 strains were obtained from infected individuals and have been described previously[15,50]. Infectious stocks were propagated by inoculating Vero-hACE2-TMPRSS2 cells. Supernatant was collected, aliquoted and stored at −80 °C. All work with infectious SARS-CoV-2 was performed in Institutional Biosafety Committee-approved BSL3 and A-BSL3 facilities at Washington University School of Medicine using positive pressure air respirators and protective equipment. All virus stocks were deep-sequenced after RNA extraction to confirm the presence of the anticipated substitutions.

Mouse experiments

Animal studies were carried out in accordance with the recommendations in the Guide for the Care and Use of Laboratory Animals of the National Institutes of Health. The protocols were approved by the Institutional Animal Care and Use Committee at the Washington University School of Medicine (assurance number A3381-01). Virus inoculations were performed under anesthesia that was induced and maintained with ketamine hydrochloride and xylazine, and all efforts were made to minimize animal suffering.

Heterozygous K18-hACE C57BL/6J mice (strain: 2B6.Cg-Tg(K18-ACE2)2Prlmn/J) were obtained from The Jackson Laboratory. Animals were housed in groups and fed standard chow diets. Eight-week-old female mice were administered 10^3 FFU of SARS-CoV-2 via intranasal administration.

Measurement of viral burden

Tissues were weighed and homogenized with zirconia beads in a MagNA Lyser instrument (Roche Life Science) in 1,000 µl of DMEM media supplemented with 2% heat-inactivated FBS. Tissue homogenates were clarified by centrifugation at 10,000*g* for 5 min and stored at −80 °C. RNA was extracted using the MagMax mirVana Total RNA isolation kit (Thermo Fisher Scientific) on a Kingfisher Flex extraction robot (Thermo Fisher Scientific). RNA was reverse transcribed and amplified using the TaqMan RNA-to-CT 1-Step Kit (Thermo Fisher Scientific). Reverse transcription was carried out at 48 °C for 15 min followed by 2 min at 95 °C. Amplification was accomplished over 50 cycles as follows: 95 °C for 15 s and 60 °C for 1 min. Copies of SARS-CoV-2 *N* gene RNA in samples were determined using a previously published assay[11,51]. Briefly, a TaqMan assay was designed to target a highly conserved region of the *N* gene (forward primer, 5′-ATGCTGCAATCGTGCTACAA-3′; reverse primer, 5′-GACTGCCGCCTCTGCTC-3′; probe, 5′-/56-FAM/TCAAGGAAC/ZEN/AACATTGCCAA/3IABkFQ/-3′). This region was included in an RNA standard to allow for copy number determination down to 10 copies per reaction. The reaction mixture contained final concentrations of primers and probe of 500 and 100 nM, respectively.

Cytokine and chemokine protein measurements

Lung homogenates were incubated with Triton-X-100 (1% final concentration) for 1 h at room temperature to inactivate SARS-CoV-2. Homogenates were analyzed for cytokines and chemokines by Eve Technologies Corporation using their Mouse Cytokine Array/Chemokine Array 31-Plex (MD31) platform.

Authentic virus neutralization assay

Serial dilutions of DARPins were incubated with 10^2 FFU of the indicated SARS-CoV-2 strains for 1 h at 37 °C. DARPin-virus complexes were added to Vero-hACE2-TMPRSS2 cell monolayers in 96-well plates and incubated at 37 °C for 1 h. Subsequently, cells were overlaid with 1% (wt/vol) methylcellulose in MEM supplemented with 2% FBS. Plates were collected 24 h later by removing overlays and fixed with 4% PFA in PBS for 20 min at room temperature. Plates were washed and sequentially incubated with an oligoclonal pool of SARS2-2, SARS2-11, SARS2-16, SARS2-31, SARS2-38, SARS2-57 and SARS2-71 antispike protein antibodies[52] and HRP-conjugated goat antimouse IgG in PBS supplemented with 0.1% saponin and 0.1% bovine serum albumin. SARS-CoV-2-infected cell foci were visualized using TrueBlue peroxidase substrate (KPL) and quantitated on an ImmunoSpot microanalyzer (Cellular Technologies). Data were processed using Prism software (GraphPad Prism 8.0).

Cryo-EM sample and grid preparation

SARS-CoV-2 S6P spike protein was produced in 293F cells and purified from cell culture supernatant using a Ni-NTA agarose column followed by Superdex S200 16/600 (GE Healthcare) size-exclusion column chromatography as described[53].

The subdomain SARS-CoV-2 RBD protein used in Cryo-EM was produced as previously described[54] with minor modification. Briefly, the DNA sequence encoding RBD residues 330–526 was cloned in a mammalian expression vector with an HRV3C cleavable single-chain Fc tag before the coding sequence. The tagged RBD protein was expressed by transient transfection in FreeStyle 293 for 6 d. The desired protein in culture supernatant was captured by protein A resin and liberated

by HRV3C cleavage. Finally, the subdomain RBD protein was purified on a Superdex 200 16/600 gel filtration column equilibrated with PBS.

The S309 IgG[32] was expressed by transient transfection in Expi293F cells for 5 d at 37 °C and purified with Protein A Sepharose Fast Flow resin (Cytiva). The DNA encoding CR3022 IgG[55] was cloned into a pVRC8400 vector with the addition of the HRV3C protease-cleavage site in the hinge region of IgG1 and expressed by transient transfection in Expi293F cells for 5 d at 37 °C and purified with protein A resin. The S309 Fab was cleaved from the S309 IgG using endoproteinase LysC (New England Biolab), and the CR3022 Fab was cleaved from CR3022 IgG with altered hinge with HRV3C protease. Protein A resin was then added to each mixture to remove Fc, and Fab was collected in the flowthrough and further purified on a Superose 6 10/300 SEC column (Cytiva) with X1 PBS (Gibco).

To generate SARS-CoV-2 S6P and FSR16m (or FSR22) complexes, SARS-CoV-2 S6P and FSR16m (or FSR22) were incubated in 1:3 molar ratio and the complexes were purified by Superdex S200 GL 10/300 (GE Healthcare) using 10 mM HEPES, 7.4, 150 mM NaCl as running buffer and were confirmed by SDS–PAGE and negative stain EM. To make RBD:SR22:S309Fab:CR3022Fab and RBD:SR16m:S309Fab:CR3022Fab ternary complexes, we incubated RBD (330–526) with molar excess of either SR22, C309 Fab and CR3022 Fab, or SR16m, S309 Fab and CR3022 Fab. 2.7 µl of the complexes at 1 mg ml^{-1} concentration in 10 mM HEPES, 7.4, 150 mM NaCl were deposited on Quantifoil R2/2 grids (quantifoil.com). Grids were vitrified using an FEI Vitrobot Mark IV (Thermo Fisher Scientific) with a wait time of 30 s, blot times of 1.5–4.5 s and blot force of 1.

Cryo-EM data collection and processing

The FSR22/SARS-CoV-2 S 6P and FSR16m/SARS-CoV-2 S 6P complexes grids were imaged using a Titan Krios electron microscope equipped with a Gatan K3 Summit direct detection device. Movies were collected at ×105,000 magnification over a defocus range of −1.0 to −2.25 µm for 2.3 s with the total dose of 40.02 $e^{-}/Å^2$ fractionated over 40 raw frames. Single particle cryo-EM data were collected with Latitude S. All data processing was done with cryoSPARCv3.3.1 (ref. [56]). Motion correction and CTF estimation in patch mode, blob particle picking and particle extraction with the box size of 500 Å for the FSR22 (or FSR16m) : SARS-CoV-2 spike complexes and 230 Å for the RBD:SR22 (or SR16m):S309 Fab: CR3022 Fab complexes were performed followed by 2D classifications, ab initio 3D reconstruction, and multiple rounds of 3D heterogeneous refinement. C3 symmetry was applied for the final reconstruction of the FSR22/FSR16m: SARS-CoV-2 spike complex after the initial 3D heterogeneous refinement using C1 symmetry identified a trimer with three RBD-up conformation bound three SR22 (or SR16m) molecules. To define RBD–FSR22 interface (Supplementary Figs. 12 and 13), local refinement was performed using a soft mask covering one SR22 and one RBD molecule. The parameters for data collection and processing were summarized in Supplementary Table 2.

Model building and refinement

Coordinates from PDB 7BNO and the initial models of SR22/SR16m generated using AlphaFold were used for the initial fit to the reconstructed maps. To build S309 Fab and CR3022 Fab, PDB 7TN0 and 6YLA were used, respectively. Then, the models were manually built using Coot.v0.9.8.1 (ref. [57]) followed by simulated annealing and real space refinement in Phenix v1.20.1-4487 (ref. [58]) iteratively. Geometry and map fitting were evaluated throughout the process using Molprobity[59] and EMRinger v1.0.0 (ref. [60]). Figures were generated using PyMOL v2.4.2 (www.pymol.org) and UCSF ChimeraX.v1.3.

Reporting summary

Further information on research design is available in the Nature Research Reporting Summary linked to this article.

Data availability

Datasets (raw data) underlying the figures have been provided as Source Data. Cryo-EM density maps and the atomic coordinates for the reported structures have been deposited to the Electron Microscopy Data Bank under accession codes EMD-26200, EMD-26201, EMD-27749 and EMD-27750, and to the PDB under accession codes 7TYZ, 7TZ0, 8DW2 and 8DW3. Source data are provided with this paper.

References

40. Steiner, D., Forrer, P. & Pluckthun, A. Efficient selection of DARPins with sub-nanomolar affinities using SRP phage display. *J. Mol. Biol.* **382**, 1211–1227 (2008).
41. Simeon, R. et al. Selection and characterization of ultrahigh potency designed ankyrin repeat protein inhibitors of *C. difficile* toxin B. *PLoS Biol.* **17**, e3000311 (2019).
42. Kondo, T. et al. Antibody-like proteins that capture and neutralize SARS-CoV-2. *Sci. Adv.* **6**, eabd3916 (2020).
43. Peng, Z. et al. Designed ankyrin repeat protein (DARPin) neutralizers of tcdb from clostridium difficile ribotype 027. *mSphere* **4**, e00596-19 (2019).
44. Tada, T. et al. Partial resistance of SARS-CoV-2 delta variants to vaccine-elicited antibodies and convalescent sera. *iScience* **24**, 103341 (2021).
45. Hoffmann, M. et al. SARS-CoV-2 cell entry depends on ACE2 and TMPRSS2 and is blocked by a clinically proven protease inhibitor. *Cell* **181**, 271–280 (2020).
46. Schmidt, F. et al. Measuring SARS-CoV-2 neutralizing antibody activity using pseudotyped and chimeric viruses. *J. Exp. Med.* **217**, e20201181 (2020).
47. Ku, Z. et al. Molecular determinants and mechanism for antibody cocktail preventing SARS-CoV-2 escape. *Nat. Commun.* **12**, 469 (2021).
48. Zang, R. et al. TMPRSS2 and TMPRSS4 promote SARS-CoV-2 infection of human small intestinal enterocytes. *Sci. Immunol.* **5**, eabc3582 (2020).
49. VanBlargan, L. A. et al. A potently neutralizing SARS-CoV-2 antibody inhibits variants of concern by utilizing unique binding residues in a highly conserved epitope. *Immunity* **54**, 2399–2416 (2021).
50. Case, J.B. et al. Resilience of S309 and AZD7442 monoclonal antibody treatments against infection by SARS-CoV-2 Omicron lineage strains. *Nat. Commun.* **13**, 3824 (2022).
51. Hassan, A. O. et al. A SARS-CoV-2 infection model in mice demonstrates protection by neutralizing antibodies. *Cell* **182**, 744–753 e744 (2020).
52. Vanblargan, L. et al. *A Potently Neutralizing Anti-SARS-CoV-2 Antibody Inhibits Variants of Concern by Binding a Highly Conserved Epitope* (Cold Spring Harbor Laboratory, 2021).
53. Olia, A. S. et al. SARS-CoV-2 S2P spike ages through distinct states with altered immunogenicity. *J. Biol. Chem.* **297**, 101127 (2021).
54. Zhou, T. et al. Structure-based design with tag-based purification and in-process biotinylation enable streamlined development of SARS-CoV-2 spike molecular probes. *Cell Rep.* **33**, 108322 (2020).
55. ter Meulen, J. et al. Human monoclonal antibody combination against SARS coronavirus: synergy and coverage of escape mutants. *PLoS Med.* **3**, e237 (2006).
56. Punjani, A., Rubinstein, J. L., Fleet, D. J. & Brubaker, M. A. CryoSPARC: algorithms for rapid unsupervised cryo-EM structure determination. *Nat. Methods* **14**, 290–296 (2017).
57. Emsley, P. & Cowtan, K. Coot: model-building tools for molecular graphics. *Acta Crystallogr. D. Biol. Crystallogr.* **60**, 2126–2132 (2004).
58. Adams, P. D. et al. PHENIX: a comprehensive Python-based system for macromolecular structure solution. *Acta Crystallogr. D. Biol. Crystallogr.* **66**, 213–221 (2010).

59. Williams, C. J. et al. MolProbity: more and better reference data for improved all-atom structure validation. *Protein Sci.* **27**, 293–315 (2018).
60. Barad, B. A. et al. EMRinger: side chain-directed model and map validation for 3D cryo-electron microscopy. *Nat. Methods* **12**, 943–946 (2015).

Acknowledgements

Prof. P. Bieniasz (The Rockefeller University) provided the 293T clone 22 cells for pseudoparticle neutralization assays. Prof. N. Landau (New York University) provided the plasmids for Δ19 spike protein of B.1.617.2 and C.37. Dr. A. Benjamin (Texas A&M University Health Science Center) assisted with Size Exclusion Chromatography experiments. We thank M. Lee for molecular dynamics analysis of RBD complexes and members of the Structural Biology Section, Vaccine Research Center, for comments and discussions. The following reagent was obtained through BEI Resources, NIAID, NIH: Spike Glycoprotein (Stabilized) from SARS-Related Coronavirus 2, Wuhan-Hu-1 with C-Terminal Histidine and Twin-Strep Tags, Recombinant from HEK293 Cells, NR-52724; Spike Glycoprotein Receptor Binding Domain (RBD) from SARS-Related Coronavirus 2, Wuhan-Hu-1 with C-Terminal Histidine Tag, Recombinant from HEK293 Cells, NR-52306. Funding for V.C., R.S. and Z.C. was provided by the National Institutes of Health Common Fund (grant DP2AI136600 to Z.C.). Funding for J.B.C. and M.S.D. was provided by the National Institute of Allergy and Infectious Diseases, National Institutes of Health and NIH (grants: R01 AI157155 to M.S.D.) J.B.C. was supported by a Helen Hay Whitney postdoctoral fellowship. Funding for Y.D.K., J.G., D.R.H., A.S.O., M.F.B., I.-T.T. and P.D.K. was provided by the Intramural Research Program of the Vaccine Research Center, National Institute of Allergy and Infectious Diseases, National Institutes of Health. R.G.C. and L.S. were supported in part by federal funds from LEIDOS under contract 18X144Q and Bill and Melinda Gates Foundation (INV-016167). Some of this work was performed at the Columbia University Cryo-EM Center at the Zuckerman Institute. T.S. and Y.T. were supported in part with federal funds from the Frederick National Laboratory for Cancer Research, NIH, under Contract HHSN261200800001. Some of the cryo-EM datasets were collected at the National CryoEM Facility (NCEF) of the National Cancer Institute, which was, in part, supported by the National Cancer Institute's National Cryo-EM Facility at the Frederick National Laboratory for Cancer Research under contract HSSN261200800001E. Funding for Z.K., H.B., N.Z. and Z.A was provided in part by a Welch Foundation endowment by grant AU-0042-20030616 and Cancer Prevention and Research Institute of Texas (CPRIT) by grants RP150551 and RP190561 (Z.A. and N.Z.). Reagent generation in the Krammer laboratory was partially funded by the NIAID Collaborative Influenza Vaccine Innovation Centers (CIVIC) under contract 75N93019C00051 and by the NIAID Centers of Excellence for Influenza Research and Response (CEIRR) under contracts 75N93021C00014 and 75N93021C00017.

Author contributions

V.C., M.S.D., P.D.K., Z.A. and Z.C. conceived the project. V.C., M.S.D., J.G., P.D.K., Y.D.K., Z.A. and Z.C. designed the experiments and analyzed the data. V.C. engineered the DARPins, developed the screening conditions and optimized the pseudovirus assays. R.S. developed the pseudovirus assay. Y.D.K. and J.G. determined the cryo-EM structures. R.G.C., T.S. and Y.T. carried out specimen preparation and data collection. D.H., A.S.O., M.F.B. and I.-T.T. performed expression and purification of the SARS-CoV-2 spike protein and antibodies. J.B.C. characterized the activity of DARPin against authentic SARS-CoV-2 and performed mouse infection experiments. Z.K., H.B. and N.Z. performed the affinity study and analyzed data. V.C., Y.D.K., P.D.K. and Z.C. wrote the manuscript with input from all of the authors. F.K., M.S.D., P.D.K., L.S., Z.A. and Z.C. acquired the funding.

Competing interests

M.S.D. is a consultant for Inbios, Vir Biotechnology, Senda Biosciences, Moderna and Immunome. The Diamond laboratory has received unrelated funding support in sponsored research agreements from Vir Biotechnology, Moderna, and Emergent BioSolutions. F.K. has consulted for Merck, Seqirus, Curevac and Pfizer and is currently consulting for Pfizer, Third Rock Ventures, Merck and Avimex. The F.K. laboratory is also collaborating with Pfizer on animal models of SARS-CoV-2. V.C., R.S. and Z.C. have filed a patent on the sequences for the DARPins. The remaining authors declare no competing interests.

Additional information

Supplementary information The online version contains supplementary material available at https://doi.org/10.1038/s41589-022-01193-2.

Correspondence and requests for materials should be addressed to Michael S. Diamond, Peter D. Kwong, Zhiqiang An or Zhilei Chen.

Peer review information *Nature Chemical Biology* thanks Alexander Eggel and the other, anonymous, reviewer(s) for their contribution to the peer review of this work.

nature research

Corresponding author(s): Zhilei Chen, Peter D. Kwong, Michael S. Diamond, Zhiqiang An

Last updated by author(s): Sep 14, 2022

Reporting Summary

Nature Research wishes to improve the reproducibility of the work that we publish. This form provides structure for consistency and transparency in reporting. For further information on Nature Research policies, see our Editorial Policies and the Editorial Policy Checklist.

Statistics

For all statistical analyses, confirm that the following items are present in the figure legend, table legend, main text, or Methods section.

n/a	Confirmed
☐	☒ The exact sample size (*n*) for each experimental group/condition, given as a discrete number and unit of measurement
☐	☒ A statement on whether measurements were taken from distinct samples or whether the same sample was measured repeatedly
☐	☒ The statistical test(s) used AND whether they are one- or two-sided *Only common tests should be described solely by name; describe more complex techniques in the Methods section.*
☒	☐ A description of all covariates tested
☐	☒ A description of any assumptions or corrections, such as tests of normality and adjustment for multiple comparisons
☐	☒ A full description of the statistical parameters including central tendency (e.g. means) or other basic estimates (e.g. regression coefficient) AND variation (e.g. standard deviation) or associated estimates of uncertainty (e.g. confidence intervals)
☐	☒ For null hypothesis testing, the test statistic (e.g. *F*, *t*, *r*) with confidence intervals, effect sizes, degrees of freedom and *P* value noted *Give P values as exact values whenever suitable.*
☒	☐ For Bayesian analysis, information on the choice of priors and Markov chain Monte Carlo settings
☒	☐ For hierarchical and complex designs, identification of the appropriate level for tests and full reporting of outcomes
☒	☐ Estimates of effect sizes (e.g. Cohen's *d*, Pearson's *r*), indicating how they were calculated

Our web collection on statistics for biologists contains articles on many of the points above.

Software and code

Policy information about availability of computer code

Data collection	Single particle cryo-EM data were collected with Leginon and Latitude S. Gen5 3.05 was used to collect luminescence data, Unicorn 6.3 was used to collect SEC data. Octet Data Acquisition 9.0 was used to collect BLI binding data; SoftMax Pro 6.5.1 was used to collect the ELISA data.
Data analysis	Graphpad prism 8 is used for data process of authentic virus and pseudoparticle neutralization assays and the in vivo studies. Cryo-EM data were processed with cryoSPARC v3.3 and models were built with Coot v0.9.8.1) and refined with Phenix v1.20.1-4487. Structural figures were made with PyMOLv2.4.2 and ChimeraX v1.3. Geometry and map fitting were made with Molprobity (http://molprobity.biochem.duke.edu/) and EMRinger v1.0.0. All software used are noted in the methods. ForteBio Octet Data Analysis software V11.1 was used to analyze the BLI data.

For manuscripts utilizing custom algorithms or software that are central to the research but not yet described in published literature, software must be made available to editors and reviewers. We strongly encourage code deposition in a community repository (e.g. GitHub). See the Nature Research guidelines for submitting code & software for further information.

Data

Policy information about availability of data

All manuscripts must include a data availability statement. This statement should provide the following information, where applicable:

- Accession codes, unique identifiers, or web links for publicly available datasets
- A list of figures that have associated raw data
- A description of any restrictions on data availability

CryoEM structures are deposited in the protein data bank with pdb codes 7TYZ, 7TZ0, 8DW2, and 8DW3.

Field-specific reporting

Please select the one below that is the best fit for your research. If you are not sure, read the appropriate sections before making your selection.

☒ Life sciences ☐ Behavioural & social sciences ☐ Ecological, evolutionary & environmental sciences

For a reference copy of the document with all sections, see nature.com/documents/nr-reporting-summary-flat.pdf

Life sciences study design

All studies must disclose on these points even when the disclosure is negative.

Sample size	Sample size for the pseudotyped lentivirus studies were chosen based on prior publications (PMID: 12750101). The group sizes for ELISA and BLI studies were selected based on prior publication (PMID: 33106671; 31213474).The group sizes for in vivo assays were determined based on prior experience and publication (PMID: 34192518). The group sizes for ELISA and BLI studies were selected based on previous publications (PMID: 33106671; 31213474).
Data exclusions	No data was excluded for the authentic virus, ELISA, animal and BLI studies. For pseudotyped lentivirus studies, gross outliers (values above or below 3 standard deviation of the mean value) were excluded from the analysis.
Replication	Replicates were used in the experiments as noted in the methods, figure legends and text
Randomization	For animal studies, mice were randomly assigned to cages and treatment groups in a age and sex-matched distribution.
Blinding	No blinding was performed although several key studies were performed and confirmed independently by other members of the group.

Reporting for specific materials, systems and methods

We require information from authors about some types of materials, experimental systems and methods used in many studies. Here, indicate whether each material, system or method listed is relevant to your study. If you are not sure if a list item applies to your research, read the appropriate section before selecting a response.

Materials & experimental systems

n/a	Involved in the study
☐	☒ Antibodies
☐	☒ Eukaryotic cell lines
☒	☐ Palaeontology and archaeology
☐	☒ Animals and other organisms
☒	☐ Human research participants
☒	☐ Clinical data
☒	☐ Dual use research of concern

Methods

n/a	Involved in the study
☒	☐ ChIP-seq
☒	☐ Flow cytometry
☒	☐ MRI-based neuroimaging

Antibodies

Antibodies used	Mouse anti-myc antibody (Invitrogen, Cat #13-2500) and HRP conjugated goat anti-mouse antibody (Jackson ImmunoResearch catalog # 115-035-146) for DARPin quantitation, HRP-conjugated goat anti-human IgG antibody (Jackson ImmunoResearch, 109-035-088) for ELISA binding studies. Mouse mAbs: SARS2-2, SARS2-11, SARS2-16, SARS2-31, SARS2-38, SARS2-57, and SARS2-71 (mouse mAbs from the Diamond laboratory); HRP-conjugated goat anti-mouse IgG (Sigma, A8924, 1:1000).
Validation	All primary mAbs were validated using purified SARS-CoV-2 RBD or S proteins using an ELISA. All secondary antibodies were validated by the manufacturer per their associated DataSheets.

Eukaryotic cell lines

Policy information about cell lines

Cell line source(s)	293T.c22 cells are from Prof. Paul Bieniasz at Rockefeller University; Vero-hACE2-TMPRSS2 cells are from A. Creanga and B. Graham at NIH. Free Style 293F cells were purchased from Thermo Fisher Scientific.
Authentication	All cell lines were previously reported and were used by us without further authentication.
Mycoplasma contamination	Cell lines were not tested for mycoplasma contamination

Commonly misidentified lines (See ICLAC register)	No commonly misidentified cell lines were used in the study.

Animals and other organisms

Policy information about studies involving animals; ARRIVE guidelines recommended for reporting animal research

Laboratory animals	Female (8-10 week old) heterozygous K18-hACE C57BL/6J mice (strain: 2B6.Cg-Tg(K18-ACE2)2Prlmn/J) were obtained from The Jackson Laboratory and were housed in groups of 3 to 4. Photoperiod = 12 hr on:12 hr off dark/light cycle. Ambient animal room temperature was 70° F, controlled within ±2° and room humidity was 50%, controlled within ±5%.
Wild animals	The study did not involve wild animals.
Field-collected samples	This study did not involve samples collected from the field.
Ethics oversight	Institutional Animal Care and Use Committee at the Washington University School of Medicine (assurance number A3381–01)

Note that full information on the approval of the study protocol must also be provided in the manuscript.